Communication

Phasing arbitrarily sampled multidimensional NMR data

John M. Gledhill, A. Joshua Wand *

Johnson Research Foundation and Department of Biochemistry & Biophysics, University of Pennsylvania,
905 Stellar-Chance Laboratories, 422 Curie Blvd., Philadelphia, PA 19104-6059, USA

Abstract

The recent re-introduction of the two-dimensional Fourier transformation (2D-FT) has allows for the transformation of arbitrarily sampled time domain signals. In this respect, radial sampling, where two incremented time dimensions (t_1 and t_2) are sampled such that $t_1 = \tau\cos\alpha$ and $t_2 = \tau\sin\alpha$, is especially appealing because of the relatively small leakage artifacts that occur upon Fourier transformation. Unfortunately radially sampled time domain data results in a fundamental artifact in the frequency domain manifested as a ridge of intensity extending through the peak positions perpendicular to $+/-$ the radial sampling angle. Successful removal of the ridge artifacts using existing algorithms requires absorptive line shapes. Here we present two procedures for retrospective phase correction of arbitrarily sampled data.
© 2007 Elsevier Inc. All rights reserved.

1. Introduction

The high probability of degenerate frequencies in NMR spectra of complex biopolymers such as proteins presented a great barrier to detailed analysis. The combination of multidimensional NMR spectroscopy and high magnetic field strengths has overcome the resulting resonance assignment problem for proteins less than 50 kDa. Furthermore, recent advances in NMR instrumentation have largely removed sensitivity as a limiting parameter for protein samples in the millimolar concentration range. As a consequence, the orthogonal linear sampling requirements of conventional multidimensional NMR spectroscopy have required longer acquisition times than potentially needed with respect to signal-to-noise. A number of approaches have been introduced to escape the linear sequential sampling requirements of the standard fast Fourier transform usually employed to deal with processing of the time domain NMR signal [1]. Many

of the new approaches find their roots in the so-called accordion spectroscopy introduced by Bodenhausen and Ernst over two decades ago where two or more incremented time domains are linked [2].

Recently the two-dimensional Fourier transformation (2D-FT) has been re-introduced to transform arbitrarily sampled time domain signals [3–5]. In principle the 2D-FT allows the use of non-linear time domain sampling. In this respect, the so-called radial sampling protocol, where two incremented time dimensions (t_1 and t_2) are sampled such that $t_1 = \tau\cos\alpha$ and $t_2 = \tau\sin\alpha$, is especially appealing because of the absence of the aliasing artifacts of random sampling that occur upon Fourier transformation. However, transformation of radially sampled time domain data results in a fundamental artifact manifested as a ridge of intensity extending through the peak positions perpendicular to $+/-$ the radial sampling angle. A number of algorithms have been introduced to remove these ridges [6–8] but, as we will emphasize below, successful removal of the ridge artifacts requires absorptive line shapes. Unfortunately, no general procedure for phasing radially sampled NMR data has been presented. Indeed, the emphasis thus

---

* Corresponding author. Fax: +1 215 573 7290.
  E-mail address: wand@mail.med.upenn.edu (A.J. Wand).

far has been on the collection of time domain data that is free of phase distortion or error. Obviously a procedure for retrospective phase correction of radially sampled data is a distinct advantage. Here we present two methods capable of phase correcting arbitrarily sampled NMR data as a solution to this problem.

2. Theory

The discrete 2D-FT can be described as [3–5,9]:

$$S(\omega_1, \omega_2) = \sum_{t_1=0}^{t_1^{\max}} \sum_{t_2=0}^{t_2^{\max}} \exp(-i\omega_1 t_1)$$
$$\times \exp(-j\omega_2 t_2) f(t_1, t_2) g(t_1, t_2) w(t_1, t_2) \quad (1)$$

where i and j are quarternion numbers; t_1 and t_2 are the incremented times, ω_1 and ω_2 comprise the frequency pair being determined, $f(t_1, t_2) = \exp(-i\Omega_1 t_1)\exp(-j\Omega_2 t_2)$ is the data being transformed, Ω_1 and Ω_2 are the chemical shifts for time domain t_1 and t_2, respectively, $w(t_1, t_2)$ is a weighting factor to account for the unequally spaced sampling of the time domain and is typically applied as a two-dimensional apodization function, and $g(t_1, t_2)$ describes the lifetime of the signal, which we will subsequently ignore. In the case of radial sampling $t_1 = \tau \cos \alpha$ and $t_2 = \tau \sin \alpha$ where τ is the incremented time and α is the sampling angle.

In accordance with standard Fourier transform quadrature theory, if the carrier frequency is set in the middle of the spectral ranges, eight pieces of data must be collected in order to determine the sign of the frequency components for a three-dimensional spectrum. Typically the proton dimension is processed separately; therefore we will only deal with the indirect evolution terms here. This simplification leaves four terms that are modulated by a mixture of cosine and sine as presented below.

$$f_{CC}(t_1, t_2) = \cos(t_1 \Omega_1) \cos(t_2 \Omega_2) \quad (2a)$$
$$f_{CS}(t_1, t_2) = \cos(t_1 \Omega_1) \sin(t_2 \Omega_2) \quad (2b)$$
$$f_{SC}(t_1, t_2) = \sin(t_1 \Omega_1) \cos(t_2 \Omega_2) \quad (2c)$$
$$f_{SS}(t_1, t_2) = \sin(t_1 \Omega_1) \sin(t_2 \Omega_2) \quad (2d)$$

Four real Fourier transformations can be used to process the four data sets, which we term the cos–cos Fourier transform (CC-FT), the cos–sin Fourier transform (CS-FT), the sin–cos Fourier transform (SC-FT) and the sin–sin Fourier transform (SS-FT). The CC-FT is used to transform the cos–cos modulated data set [Eq. (2a)], the CS-FT to transform the cos–sin modulated data set [Eq. (2b)], and so on. For example, the CC-FT becomes:

$$S_{CC}(\omega_1, \omega_2) = \sum_{t_1=0}^{t_1^{\max}} \sum_{t_2=0}^{t_2^{\max}} \cos(t_1 \omega_1)$$
$$\times \cos(t_2 \omega_2) f(t_1, t_2) w(t_1, t_2) \quad (3)$$

The three remaining transformations are similarly defined [3,9]. In order to select the appropriate quadrature image the four resulting spectra, $S_{CC}(\omega_1, \omega_2)$, $S_{CS}(\omega_1, \omega_2)$,

$S_{SC}(\omega_1, \omega_2)$ and $S_{SS}(\omega_1, \omega_2)$ are summed, canceling the quadrature images and artifact peaks.

$$S_{RR}(\omega_1, \omega_2) = S_{CC}(\omega_1, \omega_2) + S_{CS}(\omega_1, \omega_2)$$
$$+ S_{SC}(\omega_1, \omega_2) + S_{SS}(\omega_1, \omega_2) \quad (4)$$

To demonstrate the four Fourier transforms and summing procedure, we use four computer generated radially sampled time domain data sets modulated by a mixture of cos and sin as dictated by Eqs. (2a)–(2d) with one peak. The peak position for the data sets was set at (−300 Hz, 75 Hz) and the sampling angle set to 45°. The linewidth was adjusted to 10 Hz by multiplying the data sets by an exponential decay. The data sets were Fourier transformed with their respective transform as outlined by Eq. (3). Sixteen peaks are visible in the $S_{CC}(\omega_1, \omega_2)$ spectrum. Four peaks are the quadrature images at ±300, ±75 Hz and the twelve arise from intersection of the ridge artifact appearing at ±400, 0; ±200, 0; 0, ±300; 0, ±150, ±100, ±225. The other three spectra $S_{CS}(\omega_1, \omega_2)$, $S_{SC}(\omega_1, \omega_2)$ and $S_{SS}(\omega_1, \omega_2)$ have the same four quadrature image peaks with varying signs. The variation in signs causes the artifact patterns to change. In the case where two negative ridges intersect a negative artifact peak is present, when two ridges of varying sign intersect no peak is present. When all four spectra are summed the variations in sign of the quadrature and artifact peaks cause them to cancel resulting in a spectrum with just the authentic peaks remaining (Fig. 1).

In addition to the authentic peaks, ridges also extend from the peak at the sampling angle in the $S_{RR}(\omega_1, \omega_2)$ spectrum. Most often one wishes to remove the ridges and in the case where signal to noise is not limiting the lower value (LV) algorithm is preferred [6]. Here multiple data sets are collected at various sampling angles and the data is Fourier transformed independently. Subsequent to the transforms the intensities of multiple $S_{RR}(\omega_1, \omega_2)$ spectra are compared point-wise and the smallest magnitude value at each point is kept in a separate spectrum. If a sufficient number of angle data sets are collected a final spectrum free of ridges is generated.

Providing the data is free of phase error, the above Fourier transform method combined with the lower value algorithm works quickly and accurately to generate a ridge-free frequency spectrum. However, this approach is severely limited by its inability to deal with phase distorted data. If a phase error is present the lowest value algorithm will delete authentic peaks. This occurs because the lineshape of dispersive peaks causes the intensity to be zero inside the linewidth of the peak. The zero values are different for each sampling angle, therefore when multiple angles are compared by the LV algorithm the peak will be eliminated.

In order to circumvent this shortcoming, the current strategy is to optimize data collection to reduce phase distortions. Nevertheless, non-ideal spectrometer performance and inherent limitations of pulse sequences often preclude
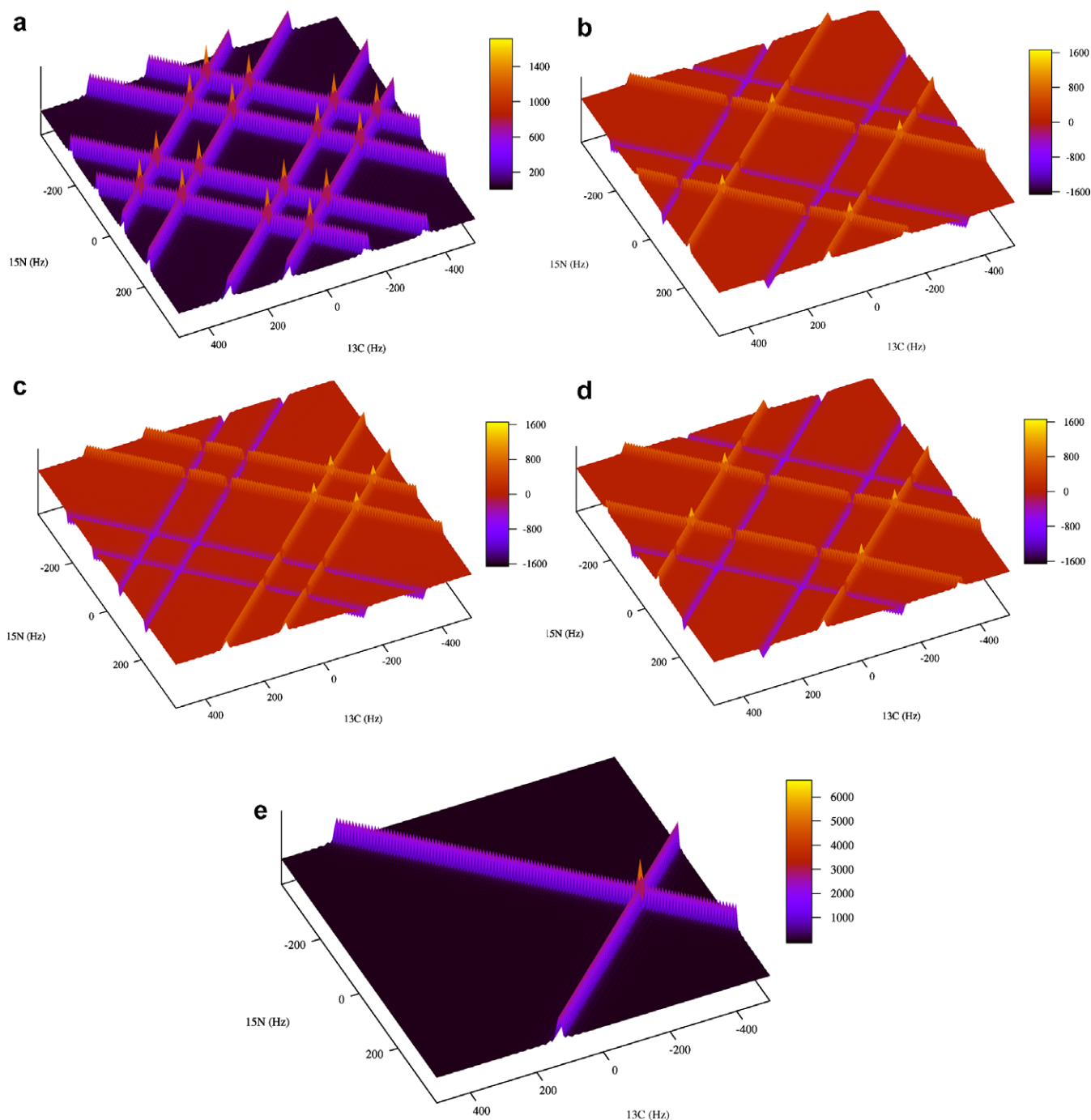
Fig. 1. An example of how quadrature images are resolved for radially sampled data processed with a single step two-dimensional Fourier transform. The data was computer generated with spectral parameters similar to that found in a radial sampled HNCO experiment. Four data sets (a–d) were generated according to Eqs. (7a), (7b), (8). The sweep widths were set to 2000 and 1500 Hz for the t_1 (carbon) and t_2 (nitrogen) dimensions, respectively. One peak was simulated at −300, 75 Hz with a linewidth of 10 Hz. Radial sampling was realized by incrementing the time in the first dimension as $t_1 = (n/sw_1)\cos\alpha$ and the second dimension as $t_2 = (n/sw_2)\sin\alpha$. The four data sets were processed with their matching Fourier transform, for example the cos–cos modulated data set was processed with the CC-FT (a), sin–cos with the SC-FT (b), cos–sin with the CS-FT (c), and sin–sin with the SS-FT (d). Inset (e) shows the sum of (a–d), resolving the appropriate quadrature image.

the collection of time domain data free of phase error. Because of the effective convolution of phase error across the various incremented time domains traditional approaches to phase correction are not applicable for radially collected data. As we will illustrate below, the presence of phase distortions severely degrade the quality of the resulting spectrum.

To solve this problem we have developed two novel phase correction methods. The first method presents a correction that is applied in the frequency domain by

generating absorptive and dispersive components with the 2D-FT. The second method applies corrections by adding constants to the 2D-FT, essentially applying a correction in the time domain.

The phase corrections in the frequency domain are applied by utilizing properties of the discrete Fourier transform to generate absorptive and dispersive components. Namely an absorptive spectrum is generated by applying a real cos Fourier transform to cos modulated data and a dispersive spectrum is generated if a real sin Fourier transform is applied to the same cos modulated data.

In the case of the 2D Fourier transform we can generate four spectra: real–real, absorptive with respect to both the ω_1 and ω_2, frequency domains, real–imaginary, absorptive with respect to the ω_1 and dispersive with respect to ω_2, and so on. The process for generating these components is summarized in Table 1. For example, the pure absorption spectrum, $S_{RR}(\omega_1,\omega_2)$, is generated by transforming the four data components with the matching Fourier transforms. That is, the cos–cos modulated data is transformed with the CC-FT, the sin–cos modulated data set is transformed with the SC-FT, the cos–sin with the CS-FT and the sin–sin with the SS-FT. The four resulting spectra are summed producing the $S_{RR}(\omega_1,\omega_2)$ spectrum. Similar procedures lead to the remaining three necessary spectra: $S_{RI}(\omega_1,\omega_2)$, $S_{IR}(\omega_1,\omega_2)$ and $S_{II}(\omega_1,\omega_2)$.

The four resulting spectra are shown in Fig. 2 for the one peak generated data set with a sample angle of 45°.

Table 1
Creation of pure and imaginary components

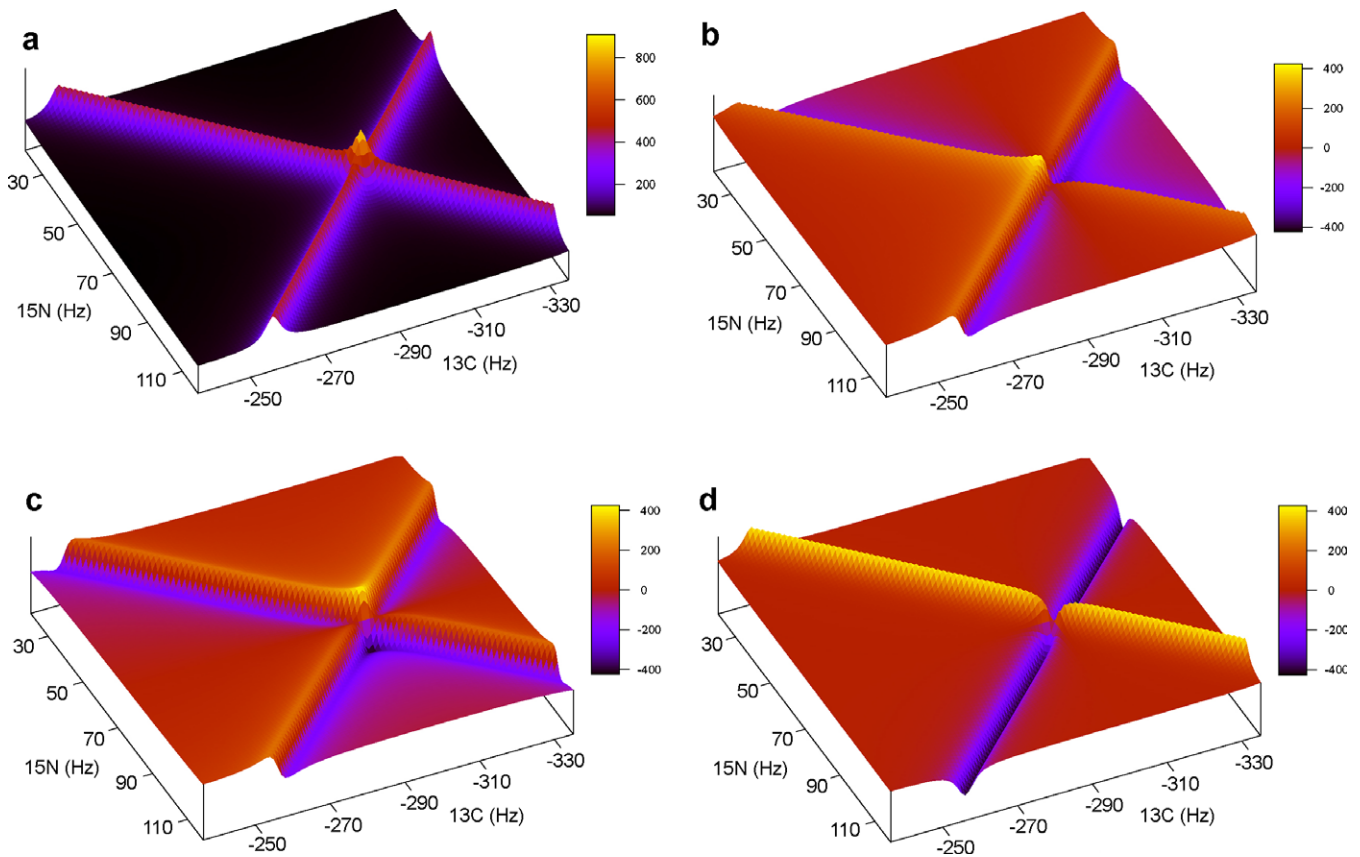|	RR	RI	IR	II
$f_{CC}(t_1,t_2)$	$\overset{CCFT}{\to} S_{CC}^{RR}(\omega_1,\omega_2)$	$\overset{CSFT}{\to} S_{CC}^{RI}(\omega_1,\omega_2)*-1$	$\overset{SCFT}{\to} S_{CC}^{IR}(\omega_1,\omega_2)$	$\overset{SSFT}{\to} S_{CC}^{II}(\omega_1,\omega_2)*-1$
$f_{CS}(t_1,t_2)$	$\overset{CSFT}{\to} S_{CS}^{RR}(\omega_1,\omega_2)$	$\overset{CCFT}{\to} S_{CS}^{RI}(\omega_1,\omega_2)*-1$	$\overset{SSFT}{\to} S_{CS}^{IR}(\omega_1,\omega_2)*-1$	$\overset{SCFT}{\to} S_{CS}^{II}(\omega_1,\omega_2)$
$f_{SC}(t_1,t_2)$	$\overset{SCFT}{\to} S_{SC}^{RR}(\omega_1,\omega_2)$	$\overset{SSFT}{\to} S_{CC}^{RI}(\omega_1,\omega_2)$	$\overset{CCFT}{\to} S_{SC}^{IR}(\omega_1,\omega_2)$	$\overset{CSFT}{\to} S_{SC}^{II}(\omega_1,\omega_2)$
$f_{SS}(t_1,t_2)$	$\overset{SSFT}{\to} S_{SS}^{RR}(\omega_1,\omega_2)$	$\overset{SCFT}{\to} S_{SS}^{RI}(\omega_1,\omega_2)$	$\overset{CSFT}{\to} S_{SS}^{IR}(\omega_1,\omega_2)*-1$	$\overset{CCFT}{\to} S_{SS}^{II}(\omega_1,\omega_2)*-1$
$\sum$	$S_{RR}(\omega_1,\omega_2)$	$S_{RI}(\omega_1,\omega_2)$	$S_{IR}(\omega_1,\omega_2)$	$S_{II}(\omega_1,\omega_2)$

Fig. 2. An example of how the 2D-FT can be used to generate absorptive and dispersive spectra with respect to $t_1(\omega_1)$ and $t_2(\omega_2)$. Inset (a) shows the real–real spectra, $S_{RR}(\omega_1,\omega_2)$, generated when the matching Fourier transform is used, i.e. CC-FT for cos–cos modulated data. Inset (b) shows the imaginary-real spectra, $S_{IR}(\omega_1,\omega_2)$, generated by not matching the FT with respect $t_1(\omega_1)$ while matching it with respect to $t_2(\omega_2)$, i.e. SC-FT for cos–cos modulated data. Insets (c and d) show the other two spectra that can be generated $S_{RI}(\omega_1,\omega_2)$ and $S_{II}(\omega_1,\omega_2)$, respectively. Table 1 outlines the complete procedure. The data was generated in the same way as in Fig. 1 and plotted to view only the area centered on the peak at −300, 75 Hz.

From initial inspection it might appear that these four spectra are sufficient to allow for phasing the two-dimensional spectrum. This is not the case. The signs of the phase correction relative to the $+\alpha$ and $-\alpha$ ridges are opposite and requires that the $+\alpha$ and $-\alpha$ components be isolated and phased separately.

The $+\alpha$ and $-\alpha$ real and imaginary components are generated by taking combinations of $S_{RR}(\omega_1, \omega_2)$, $S_{RI}(\omega_1, \omega_2)$, $S_{IR}(\omega_1, \omega_2)$ and $S_{II}(\omega_1, \omega_2)$ as shown below.

$$R^{-\alpha} = S_{RR}(\omega_1, \omega_2) + S_{II}(\omega_1, \omega_2) \tag{5a}$$

$$I^{-\alpha} = S_{IR}(\omega_1, \omega_2) - S_{RI}(\omega_1, \omega_2) \tag{5b}$$

$$R^{+\alpha} = S_{RR}(\omega_1, \omega_2) - S_{II}(\omega_1, \omega_2) \tag{6a}$$

$$I^{+\alpha} = S_{IR}(\omega_1, \omega_2) + S_{RI}(\omega_1, \omega_2) \tag{6b}$$

The $\pm\alpha$ real and imaginary components are illustrated in Fig. 3.

With the real and imaginary components of $+\alpha$ and $-\alpha$ separated the two phased spectra can finally be generated and subsequently summed to produce a phase corrected spectrum, i.e.

$$S^{+\alpha}(\omega_1, \omega_2) = R^{+\alpha} \cos\left(\phi_0^{t_1} + \phi_0^{t_2} + \phi_1^{t_1} \frac{2(\omega_1 - \omega_1^{\text{pivot}})}{sw_1} \right.$$
$$\left. - \phi_1^{t_2} \frac{2(\omega_2 - \omega_2^{\text{pivot}})}{sw_2} \right)$$
$$+ I^{+\alpha} \sin\left(\phi_0^{t_1} + \phi_0^{t_2} + \phi_1^{t_1} \frac{2(\omega_1 - \omega_1^{\text{pivot}})}{sw_1} \right.$$
$$\left. - \phi_1^{t_2} \frac{2(\omega_2 - \omega_2^{\text{pivot}})}{sw_2} \right) \tag{7a}$$

$$S^{-\alpha}(\omega_1, \omega_2) = R^{-\alpha} \cos\left(\phi_0^{t_2} - \phi_0^{t_1} + \phi_1^{t_1} \frac{2(\omega_1 - \omega_1^{\text{pivot}})}{sw_1} \right.$$
$$\left. + \phi_1^{t_2} \frac{2(\omega_2 - \omega_2^{\text{pivot}})}{sw_2} \right)$$
$$+ I^{-\alpha} \sin\left(\phi_0^{t_2} - \phi_0^{t_1} + \phi_1^{t_1} \frac{2(\omega_1 - \omega_1^{\text{pivot}})}{sw_1} \right.$$
$$\left. + \phi_1^{t_2} \frac{2(\omega_2 - \omega_2^{\text{pivot}})}{sw_2} \right) \tag{7b}$$

where $\phi_0^{t_1}$, $\phi_0^{t_2}$, $\phi_1^{t_1}$ and $\phi_1^{t_2}$ are the t_1 and t_2 zero and first order corrections. Also note that a factor of two was included in the first order terms to make setting the first order
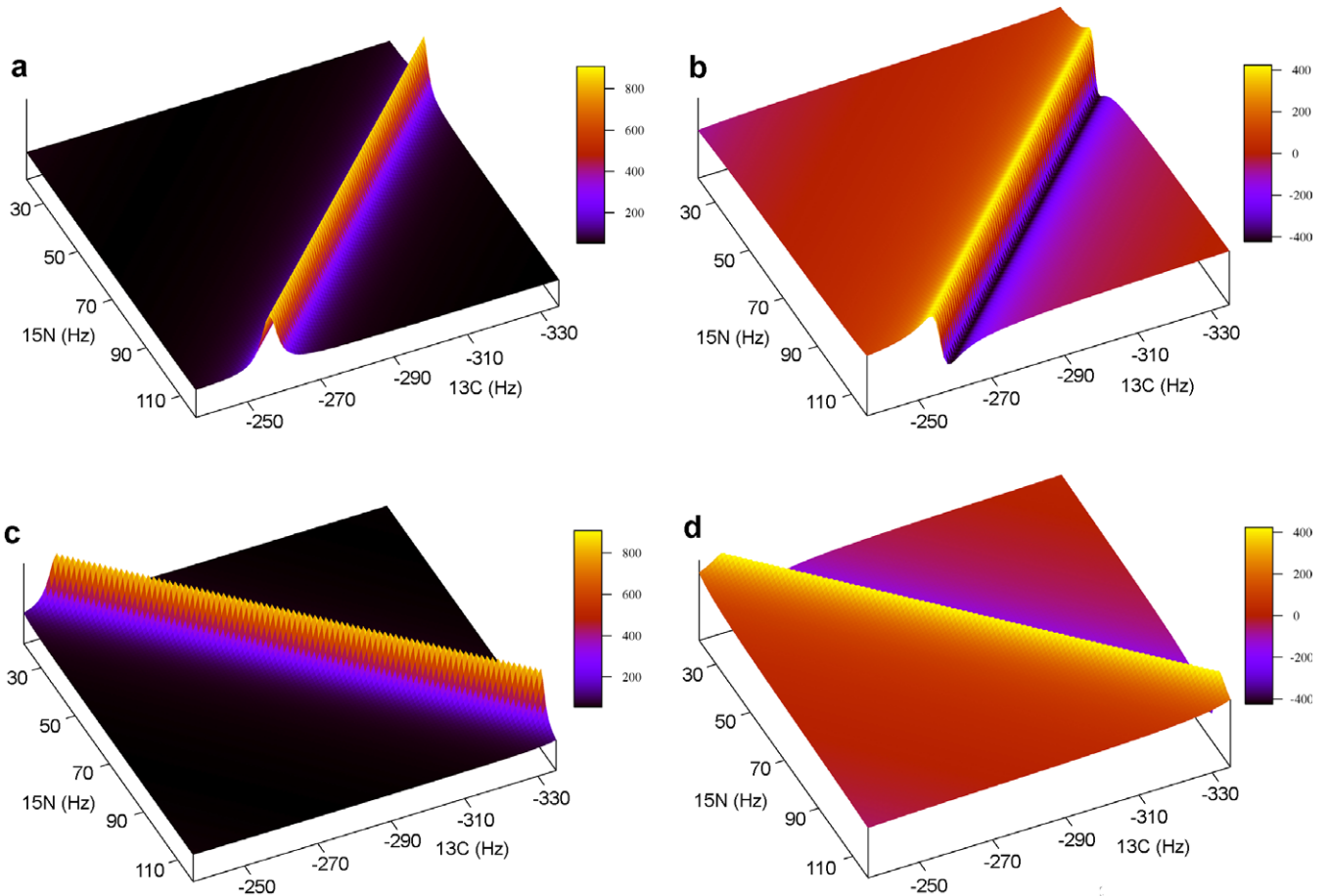

Fig. 3. An example of the pure $\pm\alpha$ real and imaginary component spectra used for phase correction in the frequency domain. Insets (a and b) show the real and imaginary $+\alpha$ spectra, while insets (c and d) show the real and imaginary $-\alpha$ spectra. Combinations of the $+\alpha$ and $-\alpha$ components are generated independently and subsequently summed to produce a phased spectrum.

correction independent of the zero order terms. For example, if the pivot is set in the middle of the spectrum and one adds a half dwell to the incremented time period $\pm 90°$ phase corrections are needed at the edges of the spectrum. Traditionally the zero and first order phase corrections are set to $90°$, $-180°$. By including the factor of two the phases can be set to $0°$, $-90°$. Therefore only one parameter needs to be adjusted if only a first order phase correction needs to be applied.

To generate a final spectrum, the $S^{+\alpha}$ and $S^{-\alpha}$ are summed [Eq. (8)].

$$S(\omega_1, \omega_2) = S^{+\alpha}(\omega_1, \omega_2) + S^{-\alpha}(\omega_1, \omega_2) \qquad (8)$$

Alternatively, the $S^{+\alpha}$ and $S^{-\alpha}$ can be used separately in the lower value-back projection algorithm [7]. This would give an advantage over summing the spectra because more combinations would be available for comparison.

Practically, the zero and first order phase corrections are empirically determined from either an indirectly detected plane of the three-dimensional spectrum with a single peak, so the analysis is not confused by artifacts, or from the $0°$ and $90°$ tilt angle spectra. For the single peak case, four spectra are first generated, as outlined in Table 1. Next, the sum and difference spectra are generated as in Eqs. (5) and (6). Finally, the four phase corrections are applied as outlined in Eq. (7). Here the phases are searched for by varying each phase term until an absorptive spectrum is produced. Else the phase corrections can be determined independently from the $0°$ and $90°$ sample angle planes. The $0°$ and $90°$ sample angles allow the phase corrections to be isolated for either t_1 or t_2, respectively. In these spectra only one indirect time domain is evolved. Therefore traditional phasing techniques are applicable so the phase corrections can be determined by employing a Hilbert transform to generate the dispersive components [10]. After the phase corrections are determined from the $0°$ and $90°$ sample angle planes, they are applied to all angles using Eq. (7).

When only zero order corrections are needed it is equally feasible to determine them from a one peak plane or from the $0°$ and $90°$ tilt angle spectra. However when any first order correction needs to be applied, it is much easier to determine the phase corrections from the $0°$ and $90°$ sample angle spectra. The isolation of the t_1 and t_2 phase correction components by the $0°$ and $90°$ sample angle spectra significantly simplify the problem. It is also important to note when first order corrections are applied the ridges do not phase with the peaks. This occurs because of the frequency dependence of the first order correction. Therefore the ridges will in phase proximal to the peak but dispersive as they move further away. Although this might sound problematic, robust schemes are available to remove the ridges if the peaks are properly phased.

Phase corrections can also be applied in the time domain by adding constants to the 2D-FT [Eq. (9)].

$$S(\omega_1, \omega_2) = \sum_{t_1=0}^{t_1^{\max}} \sum_{t2=0}^{t_2^{\max}} \exp(-i\omega_1(t_1 + \phi_1^{t_1}) + \phi_0^{t_1})$$
$$\times \exp(-j\omega_2(t_2 + \phi_1^{t_1})$$
$$+ \phi_0^{t_2}) f(t_1, t_2) w(t_1, t_2) \qquad (9)$$

Here, $\phi_0^{t_1}$, $\phi_1^{t_1}$, $\phi_0^{t_2}$ and $\phi_1^{t_2}$ are the zero and first order phase corrections for the incremented time domains t_1 and t_2, respectively. This method directly extends from the definition of phase error in time domain data,

$$f_{CC}(t_1, t_2) = \cos((t_1 + \phi_1^{t_1})\Omega_1 + \phi_0^{t_1})\cos((t_2 + \phi_1^{t_2})\Omega_2 + \phi_0^{t_2}) \qquad (10)$$

and properties of the discrete Fourier transform. Namely a nonzero Fourier series coefficient is determined if the function generated by the Fourier transform matches the data function. We have simply extended this concept to include phase corrections so the function generated by the Fourier transform better matches the experimental data. In turn, an absorptive lineshape is generated upon transformation.

As above the phase corrections are determined empirically from either a plane with one peak or from the $0°$ and $90°$ sample angle spectra. Once the phase corrections are determined the data is retransformed with the appropriate corrections applied to Eq. (9).

It is important to point out that phasing in the time domain has not previously been presented because of inherent limitations of the fast Fourier transform (FFT) algorithm [11]. This can most easily be explained by first inspecting the discrete one-dimensional Fourier transform [Eq. (11)].

$$S(\omega) = \sum_{t=0}^{t^{\max}} \exp(-i\omega t) f(t) \qquad (11)$$

From inspection it is clear that N^2 operations are required to compute $S(\omega)$. This is obviously undesirable if a large number of data points are collected. However, if an extension of the Yates algorithm is applied, the N^2 operations can be reduced to $N\log_2 N$ operations [11]. This is accomplished by iteratively dividing the data to smaller and smaller groups until N groups of size 1 are present. At this point the 1 data point groups can be Fourier transformed and combined in the manner presented by Cooley and Tukey [11].

Properties of the one point Fourier transform are essential to this algorithm. In particular, the Fourier transform of one data point is itself independent of frequency. This is true because $t = 0$ and therefore $\exp(-i\omega t) = 1$ However, if phase corrections are incorporated, t is no longer equal to zero and the Fourier transform is no longer frequency independent and the FFT algorithm is no longer applicable.

3. Results

This procedure is illustrated in Fig. 4 using a standard HNCO [12] modified for radial sampling, such that
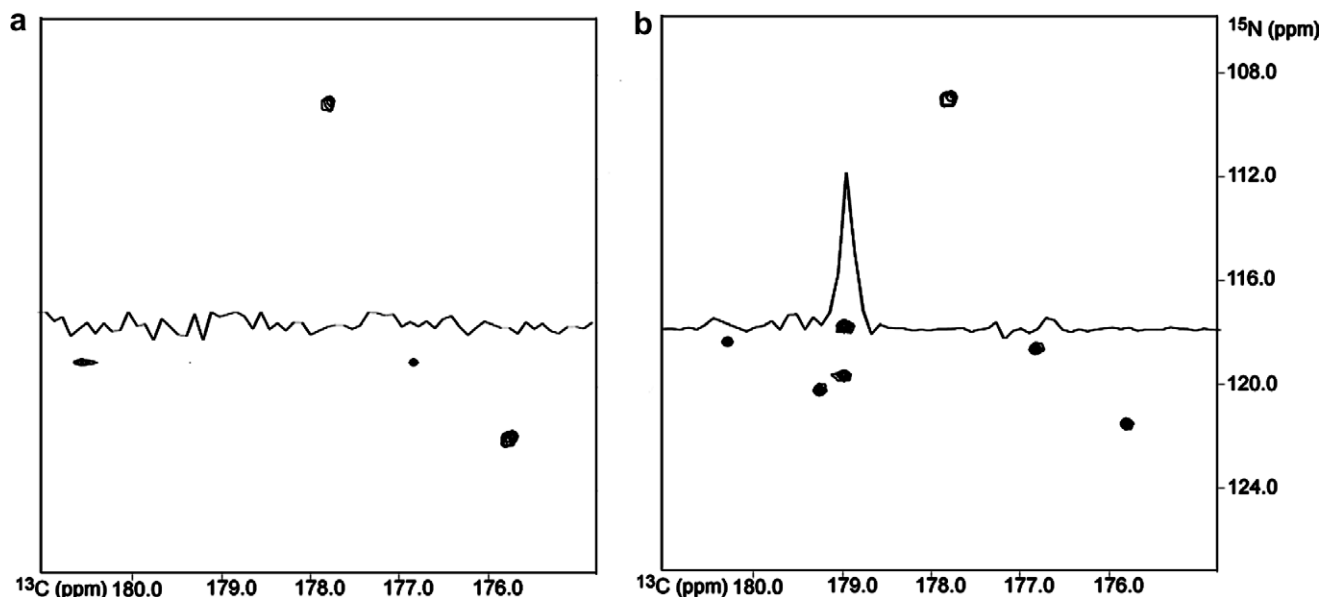
Fig. 4. Comparison of the same indirect dimension plane for a spectrum processed with no phase correction (a) and with phase correction (b). The phase corrected spectrum shows all peaks at the correct frequencies with the appropriate intensities. The spectrum with no phase correction is missing numerous peaks, as emphasized by the overlaid one-dimensional spectra. Ten sample angle data sets were collected on a 1:1 complex between calcium-saturated calmodulin and a peptide corresponding to the calmodulin binding domain of phosphodiesterase using a HNCO modified for radial sampling. The individual sampling angles were processed separately and compared using an in-house implementation of the lower-value algorithm.

$t_1 = \tau\cos(\alpha)$ and $t_2 = \tau sw_1/sw_2\sin(\alpha)$, on a 1 mM 1:1 complex between calcium-saturated calmodulin and a peptide corresponding to the calmodulin binding domain of phosphodiesterase 1A. In order to demonstrate the ability to apply a first order phase correction the experiment was setup with a half dwell added to both the t_1 and t_2 increments. Accordingly, the spectra required first order corrections of $-90°$ for both the $t_1(\omega_1)$ and $t_2(\omega_2)$ dimensions. Additionally the spectrum required a zero order correction of $36°$ in the t_1 dimension.

4. Discussion and conclusions

The need to have properly phased multidimensional frequency space data is essential to the general application of radial sampling and the 2D-FT. As demonstrated by the HNCO spectrum with no phase correction shown in Fig. 4a, when a lower magnitude comparison is performed for a data set without phase correction authentic peaks will incorrectly be removed. In many cases, phase error cannot be avoided and explicit phase correction will be required. We have devised two approaches to the phasing of such data, either by manipulation in the frequency domain or in the time domain. The choice of method, time or frequency phase correction, is dependent upon the application at hand. For example, phasing in the frequency domain will be important upon the advent of a fast 2D-FT algorithm. Whereas, phasing in the time domain will easily be implemented in higher dimensional Fourier transforms. In a similar vein, it is useful to note that the same general approach can be used in the retrospective phase correction of data obtained by projection reconstruction methods [6].

5. Methods

NMR data was collected on a ~1 mM 1:1 complex between calcium-saturated calmodulin and a peptide corresponding to the calmodulin binding domain of the phosphodiesterase at 35 °C on a Varian INOVA 600 MHz spectrometer, equipped with a triple-resonance cryogenic probe. The CaM–PDE complex was prepared in 10 mM imidazole, pH 6.5, 6 mM $CaCl_2$, 100 mM KCl and 0.04% azide. Ten sample angles were collected from $0°$ to $90°$ in $10°$ increments. Each spectrum was derived from data sets composed of 384 FIDs, four quadrature components at 96 increments. Each FID contained 1024 complex points and was the average of eight scans. The spectral width was set to 14 ppm in the proton dimension. The spectral widths for the indirect dimensions were chosen to assure no peaks were folded and set to 40 and 12 ppm in the nitrogen and carbon dimensions, respectively. The ten angle spectra were processed independently and compared using a lower magnitude algorithm to remove the ridge artifacts. All processing and comparisons were done using an in-house program.

References

[1] R. Freeman, E. Kupce, New methods for fast multidimensional NMR, J. Biomol. NMR 27 (2003) 101–113.

[2] G. Bodenhausen, R.R. Ernst, The accordion experiment, a simple approach to 3-dimensional NMR-spectroscopy, J. Magn. Reson. 45 (1981) 367–373.

[3] B.E. Coggins, P. Zhou, Polar Fourier transforms of radially sampled NMR data, J. Magn. Reson. 182 (2006) 84–95.

[4] K. Kazimierczuk, A. Zawadzka, W. Kozminski, I. Zhukov, Random sampling of evolution time space and Fourier transform processing, J. Biomol. NMR 36 (2006) 157–168.

[5] D. Marion, Processing of ND NMR spectra sampled in polar coordinates: a simple Fourier transform instead of a reconstruction, J. Biomol. NMR 36 (2006) 45–54.

[6] E. Kupce, R. Freeman, Projection-reconstruction technique for speeding up multidimensional NMR spectroscopy, J. Am. Chem. Soc. 126 (2004) 6429–6440.

[7] R.A. Venters, B.E. Coggins, D. Kojetin, J. Cavanagh, P. Zhou, (4,2)D projection-reconstruction experiments for protein backbone assignment: application to human carbonic anhydrase II and calbindin D-28K, J. Am. Chem. Soc. 127 (2005) 8785–8795.

[8] J.W. Yoon, S. Godsill, E. Kupce, R. Freeman, Deterministic and statistical methods for reconstructing multidimensional NMR spectra, Magn. Reson. Chem. 44 (2006) 197–209.

[9] K. Kazimierczuk, W. Kozminski, I. Zhukov, Two-dimensional Fourier transform of arbitrarily sampled NMR data sets, J. Magn. Reson. 179 (2006) 323–328.

[10] R.R. Ernst, Numerical Hilbert transform and automatic phase correction in magnetic resonance spectroscopy, J. Magn. Reson. 1 (1969) 7–26.

[11] J.W. Cooley, J.W. Tukey, An algorithm for machine calculation of complex Fourier series, Math. Comput. 19 (1965) 297–301.

[12] D.R. Muhandiram, L.E. Kay, Gradient-enhanced triple-resonance 3-dimensional NMR experiments with improved sensitivity, J. Magn. Reson Ser. B 103 (1994) 203–216.